Intuitive and coherent intraretinal cystoid map representation in Optical Coherence Tomography images ⋆

Plácido Vidal[1,2,*], Joaquim de Moura[1,2], Jorge Novo[1,2], Manuel G. Penedo[1,2], and Marcos Ortega[1,2]
{placido.francisco.lizancos.vidal, joaquim.demoura, jnovo, mgpenedo, mortega}@udc.es

[1] Department of Computer Science, University of A Coruña, A Coruña (Spain)
[2] CITIC - Research Center of Information and Communication Technologies, University of A Coruña, A Coruña (Spain)

Abstract. Fluid accumulations in between the retinal layers represent one of the main causes of blindness in developed countries. Currently, these fluid accumulations are detected by means of a manual inspection of Optical Coherence Tomography images, prone to subjective and non-quantifiable diagnostics. For this reason, numerous works aimed for an automated methodology. Nonetheless, these systems mostly focus on obtaining a defined segmentation, which is not always possible. For this reason, we present in this work a fully automatic methodology based in a fuzzy and confidence-based visualization of a regional analysis, allowing the clinicians to study the fluid accumulations independently of their distribution, complications and/or other artifacts that may complicate the identification process.

Keywords: Computer-aided Diagnosis · Optical Coherence Tomography · Macular Edema · Regional analysis · Visualization

1 Introduction

The retina represents the neurosensory part of the human eye. This structure comprises both an extension of the nervous and the vascular systems [6], reflecting changes that may appear in any of them in its sensitive structures. For this reason, the retina has become the focus of many Computer-aided diagnosis (CAD) systems, as it allows to obtain information about a wide-range of internal processes.

⋆ This work is supported by the Instituto de Salud Carlos III, Government of Spain and FEDER funds of the European Union through the DTS18/00136 research projects and by the Ministerio de Economía y Competitividad, Government of Spain through the DPI2015-69948-R research project. Also, this work has received financial support from the European Union (European Regional Development Fund - ERDF) and the Xunta de Galicia, Centro singular de investigación de Galicia accreditation 2016-2019, Ref. ED431G/01; and Grupos de Referencia Competitiva, Ref. ED431C 2016-047.

The main way of studying the retina is by the inspection of a medical imaging technique called Optical Coherence Tomography (OCT). This imaging modality is capable of providing a cross-sectional representation of the retinal layers in a non-invasive way. Currently, one of the most common uses for this technique is the study of intraretinal fluid accumulations. These accumulations, consequence of pathologies like the Age-Related Macular Degeneration (AMD) and the Diabetic Retinopathy (RD), are among the main causes of blindness in developed countries.

Frequently, these images are being manually analyzed by the expert ophthalmologist, assessing the severity of the pathology and its evolution by using only its expertise and experience (which may be subject to subjective variables, inter-expert discrepancy and even inter/intra device variations). For this reason, several methodologies arose trying to offer an improved alternative to this issue. These works follow a similar archetype to the one established by Wilkins *et al.* [13], mainly based on an image processing to enhance the features of the image, an initial candidate segmentation and a final false positive (FP) filtering. In the particular case of Wilkins *et al.*, this image processing is characterized by a denoising step, candidate segmentation by a fixed thresholding and candidate filtering by using shape and size rules. As an example of this tendency, Girish *et al.* [2] improved this work by using a watershed algorithm to the initial candidate listing, Chiu *et al.* [1] changed the classification to a kernel regression strategy and the FP filtering to a graph theory and dynamic programming strategy and Wang *et al.* [12] generated a 3D segmentation using subsequent OCT scans and a fuzzy C-means algorithm, but still maintaining the posterior FP filtering. Additionally, some works (like the proposal of Samagaio *et al.* [9]) have extended the segmentation approach to a characterization of these fluid accumulations into the different clinical types of macular edema.

Finally, some works focused on obtaining these segmentations using deep learning strategies. Most of these works follow an approach derived from the original (and commonly used in the analysis of medical images for obtaining a precise segmentation) U-Net architecture proposed by Ronnenberger *et al.* [8]. As an example of this, we find the works of Lee *et al.* [3], Venhuizen *et al.* [10] or Lu *et al.* [4] (albeit this last work focused in a multiclass fluid identification).

All these works present satisfactory results in the segmentation domain, but these fluid accumulations do not appear always with a defined region to segment, nor one that different experts would agree on. An example of fluid regions with confusing limits can be seen in Figure 1. As shown, these fluid regions are mixed with other pathologies, artifacts product of the imaging technique, and with normal retinal tissue. Such is this variability that establishing a common ground truth with different experts would also carry an astonishing variability, thus making it unreliable as accurate baseline.

As an alternative, de Moura *et al.* [5, 7] established other way of studying these accumulations. This approach does not look for a precise segmentation nor a full image classification. Instead, it merges both ideas to perform a regional analysis. This analysis is centered in classifying individual samples as pathological or healthy regions. With this strategy as foundation [11], in this work, we present

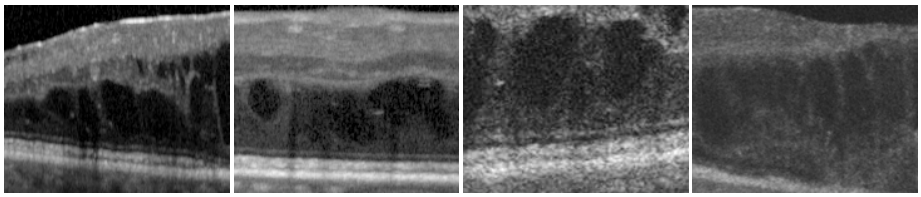

Fig. 1. Samples with diffuse fluid accumulations from OCT images that were captured by a Spectralis device and a Cirrus device.

a visualization that takes advantage of the resilience of this method in the fluid problematic areas to create intuitive detections to be analyzed by the expert clinician. Down below we will proceed to further explain each of the steps followed during this process.

2 Methodology

2.1 Retinal layer segmentation

The first step of the strategy consists in delimiting the region of interest (ROI). In particular, we focused on two differentiated retinal layers: the Inner Limiting Membrane (ILM) and the Retinal Pigment Epithelium (RPE), both representing the innermost and outermost layers of the retina, respectively.

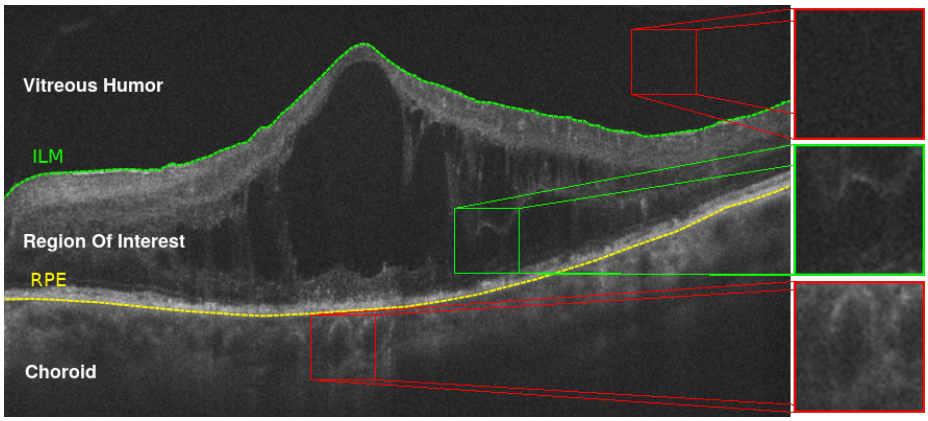

Fig. 2. Different regions considered in an OCT image and three confusing samples from each one of them. From top to bottom: choroid sample, fluid region inside the ROI and vitreous humor sample.

Just next to the ILM, we can find the vitreous humor (the fluid inside the eye); and next to the RPE, the choroid region (the vascular layer that nourishes the

outermost layers of the retina). In Figure 2, these main regions are shown with representative samples of each one of them that will illustrate and motivate why the extraction of the ROI is made. As the reader can see, the sample from the choroid and the sample from the vitreous humor can perfectly be visually confused as intraretinal fluid. The vitreous humor, being a liquid region, presents the same characteristics as the fluid leakages inside the retinal layers. The choroid, on the other hand, is a vascular network with circular diffuse patterns that perfectly mimic the ones also present in the fluid leakages. Finally, the fluid sample from the ROI shows a pattern that could be present in the retina, the vitreous humor and as well as in the choroid. For this reason, to diminish the pattern load the classifier has to learn, these regions are omitted in the posterior analysis.

2.2 Image sampling and subsample extraction

After the ROI is extracted, the image is divided in a series of overlapping samples. To extract these overlapping samples, each axis of the ROI is divided in rows and columns spaced by *Window size - Established overlap* pixels. That way, the points where these rows and columns meet, a sample center is positioned. Finally, for each one of these points, a window is extracted.

The regional analysis used in this work bases itself in the study of texture features. These features describe statistically how the pixel gray levels are spatially organized in a given sample. Nonetheless, the image sampling extracts squared samples from an irregularly-shaped ROI, resulting in some samples partially falling outside the ROI and thus containing non-relevant information that must be discarded.

As this spatial information has to be maintained and the matrices have to be rectangular, we cannot simply remove the external pixels from a resulting array. For this reason, we devised an algorithm to find the biggest rectangle inside a given sample that contains only valid pixels. Additionally, to ensure a minimum size of this subsample, only those that are centered inside the ROI will be considered. If a sample does not meet this criteria, it is simply discarded and not counted towards the final vote.

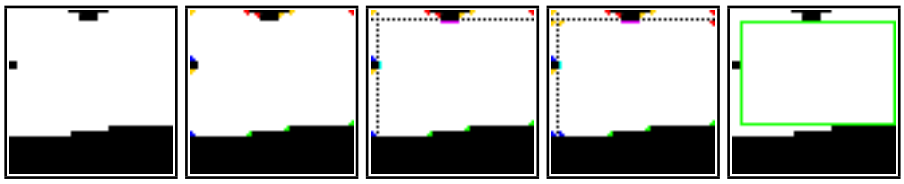

Fig. 3. Steps to extract the biggest subsample from the relevant region (in *white*). *Red: NE, Yellow: NW, Blue: SW, Green: SE, Magenta: S* and *Light Blue: E*

To extract the subsample, we first find all the possible corners these subrectangle could have (Figure 3a-b). For this, we use the *hit-or-miss* transform. This

morphological operation allows us to find points in an image that match both a pattern in the background of the image as well as the foreground. More precisely, we use the masks defined in Equation 1. Each of these masks will return a series of different points where the ROI pixels (represented in the mask by 1s) and the non-ROI pixels (represented in the mask by -1s) match those patterns. That way, the *NE* mask will signal the north-east facing corners, the *NW* mask will signal the north-west facing corners, SE the south-east ones and, finally, the *SW* will mark the south-west ones.

$$NE = \begin{pmatrix} 0 & -1 & -1 \\ 1 & 1 & -1 \\ 0 & 1 & 0 \end{pmatrix} NW = \begin{pmatrix} -1 & -1 & 0 \\ -1 & 1 & 1 \\ 0 & 1 & 0 \end{pmatrix} SE = \begin{pmatrix} 0 & 1 & 0 \\ 1 & 1 & -1 \\ 0 & -1 & -1 \end{pmatrix} SW = \begin{pmatrix} 0 & 1 & 0 \\ -1 & 1 & 1 \\ -1 & -1 & 0 \end{pmatrix} \tag{1}$$

After these corners are found, all the possible rectangles formed by any combination of the opposing corners are studied. That is, *NE* with *SW* and *NW* with *SE* (and only if they are facing each other). If the area within a pair of corners contains any pixel from the non-ROI area, that candidate is also discarded. Finally, once we have all the valid candidates, the one with the biggest area is chosen and extracted from the original sample.

In some cases, the optimum rectangle would have corners in a region without valid paired candidate corner points. That is, for example, it would have an *SE* corner but not a corresponding *NW* (represented in Figure 3 as the bottom right green corner without a matching NW). For this reason, to the previous set of detected corners, an additional set is added considering also artifacts that may create an invisible barrier. To find these candidates, the *hit-or-miss* transform is also used, but with the masks shown in Equation 2 (Figure 3c). Additionally, as these masks would return multiple detections in flat surfaces, only one of the pixels is considered per orientation and row/column. Also, as some of these regions are already covered by a previous detected corner, rows and corners with an existing previous corner will also be ignored.

$$N = \begin{pmatrix} 0 \\ 1 \\ -1 \end{pmatrix} S = \begin{pmatrix} -1 \\ 1 \\ 0 \end{pmatrix} E = \begin{pmatrix} -1 & 1 & 0 \end{pmatrix} W = \begin{pmatrix} 0 & 1 & -1 \end{pmatrix} \tag{2}$$

Considering these new invisible walls, the *hit-or-miss* looks again for candidate corners (Figure 3d). And, as shown in Figure 3e, that was precisely (in this example) where the optimum rectangle was located.

2.3 Sample voting and normalization

Finally, each of the resulting samples is classified by a previously trained model into a pathological or a non-pathological class. To convert these values into a confidence indicator, we use a voting strategy. The confidence of a given pixel is determined by the number of windows classified into the pathological class that in the original image contained that same pixel. Thanks to using this strategy,

the confidence is calculated not only by one classification, but also using the information from the neighboring samples that cover an extended region.

Nonetheless, in the ROI areas close to the borders, the number of windows that overlap the region is sensibly lower than in the internal ones. Additionally, depending on the ROI shape and size, rounding errors when calculating the sample centers will cause a lattice pattern to appear (as some pixels, product of this rounding, will be overlapped by less windows in their frontier zones). To solve this issue, the number of pixels is divided by the number of windows that overlapped that pixel. This way, the confidence is stated as the relative percentage of windows that, overlapping that given pixel, were considered as pathological. Figure 4 shows a representation of these two issues in a map where the window overlap density is represented.

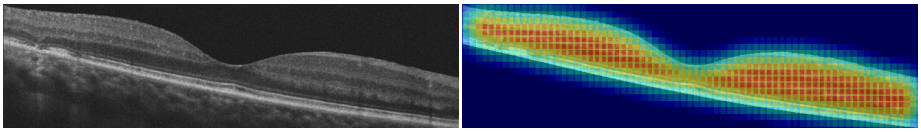

Fig. 4. Original healthy OCT image ROI and a representation over it of the vote density (overlap of 50px between samples).

2.4 Intuitive color mapping

Finally, an intuitive color map is constructed to represent the final detection; being merged with the original image. The color map presents a cold-hot scale with several and progressive hue changes. This pattern allows the expert clinician to assess the severity of a pathology and know, with a quick look, the confidence metric established by the system. Figure 5 shows a finished confidence map. As shown, with a simple gaze, a human examiner can quickly assess the confidence thanks to the proposed color scale.

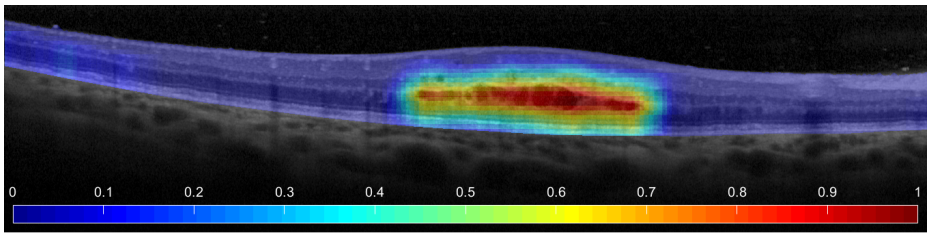

Fig. 5. Map with the corresponding color scale indicating the relationship between the color that is shown in the map and the confidence assigned by the system.

3 Results and conclusions

The map generation strategy hereby presented and the resulting visualization are able to create, from an individual OCT image, a complete and intuitive

representation of the fluid regions. Moreover, these detections are able to work even when the fluid accumulations do not present a defined border that can be segmented due to its diffuse nature.

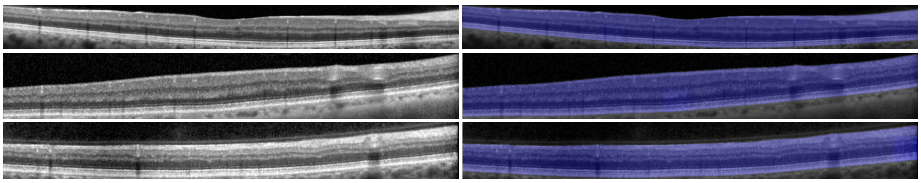

Fig. 6. Examples of healthy ROI regions without fluid leakages and their corresponding confidence maps.

Figure 6 shows an example of healthy OCT images without fluid accumulations. Even confusing artifacts like shadows that are generated by vessels or slight darkened regions product of the OCT device are explicitly and correctly identified as non-pathological.

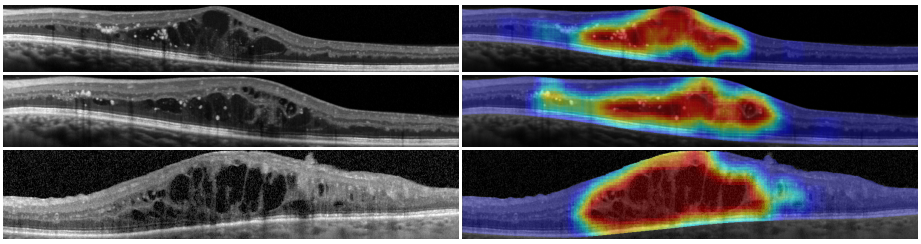

Fig. 7. Examples of ROI regions with complex fluid leakages and their corresponding confidence color maps.

On the other hand, Figure 7 presents three complex cases of fluid accumulations mixed with other pathologies and healthy tissue. The reader can easily see how, comparing with Figure 6, an expert clinician that analyzes both images could easily tell, without much inspection, which patients present relevant leakages and which ones are healthy. Additionally, this methodology is not limited to fluid accumulations or even to OCT images. By changing the classifier, the system could easily be used to detect other pathological complications in this or other different image modality (in most medical imaging systems, the ROI extraction phase can be omitted if there is no danger of confusing texture patterns between structures). Finally, we would like to remark that adapting this method also does not require a precise ground truth like a segmentation would. This model is trained by means of a binary classification of square samples, easier to do for a human expert and more robust than a segmentation-based one. That is, with vague classifications that tolerate the human margin of error we can create a coherent, intuitive and defined representation of the pathological regions.

References

1. Chiu, S.J., Allingham, M.J., Mettu, P.S., Cousins, S.W., Izatt, J.A., Farsiu, S.: Kernel regression based segmentation of optical coherence tomography images with diabetic macular edema. Biomed. Opt. Express **6**(4), 1172–1194 (Apr 2015)
2. Girish, G., Kothari, A.R., Rajan, J.: Automated segmentation of intra-retinal cysts from optical coherence tomography scans using marker controlled watershed transform. In: Engineering in Medicine and Biology Society (EMBC), 2016 IEEE 38th Annual International Conference of the. pp. 1292–1295. IEEE (2016)
3. Lee, C.S., Tyring, A.J., Deruyter, N.P., Wu, Y., Rokem, A., Lee, A.Y.: Deep-learning based, automated segmentation of macular edema in optical coherence tomography. Biomed. Opt. Express **8**(7), 3440–3448 (Jul 2017)
4. Lu, D., Heisler, M., Lee, S., Ding, G.W., Navajas, E., Sarunic, M.V., Beg, M.F.: Deep-learning based multiclass retinal fluid segmentation and detection in optical coherence tomography images using a fully convolutional neural network. Medical Image Analysis **54**, 100 – 110 (2019)
5. de Moura, J., Novo, J., Rouco, J., Penedo, M., Ortega, M.: Automatic identification of intraretinal cystoid regions in optical coherence tomography. Conference on Artificial Intelligence in Medicine in Europe - AIME'17 pp. 305–315 (2017)
6. de Moura, J., Novo, J., Ortega, M., Barreira, N., Charlón, P.: Automatic retinal vascularity identification and artery/vein classification using near-infrared reflectance retinographies. In: Computer Vision, Imaging and Computer Graphics - Theory and Applications. pp. 262–278. Springer International Publishing, Cham (2019)
7. de Moura, J., Vidal, P., Novo, J., Rouco, J., Ortega, M.: Feature definition, analysis and selection for cystoid region characterization in optical coherence tomography. In: Knowledge-Based and Intelligent Information & Engineering Systems: Proceedings of the 21st International Conference KES-2017, Marseille, France, 6-8 September 2017. pp. 1369–1377 (2017)
8. Ronneberger, O., Fischer, P., Brox, T.: U-net: Convolutional networks for biomedical image segmentation. In: Medical Image Computing and Computer-Assisted Intervention – MICCAI 2015. pp. 234–241. Springer International Publishing, Cham (2015)
9. Samagaio, G., Estévez, A., de Moura, J., Novo, J., Fernández, M.I., Ortega, M.: Automatic macular edema identification and characterization using OCT images. Computer Methods and Programs in Biomedicine **163**, 47–63 (2018)
10. Venhuizen, F.G., van Ginneken, B., Liefers, B., van Asten, F., Schreur, V., Fauser, S., Hoyng, C., Theelen, T., Sánchez, C.I.: Deep learning approach for the detection and quantification of intraretinal cystoid fluid in multivendor optical coherence tomography. Biomed. Opt. Express **9**(4), 1545–1569 (Apr 2018)
11. Vidal, P., de Moura, J., Novo, J., Penedo, M.G., Ortega, M.: Intraretinal fluid identification via enhanced maps using optical coherence tomography images. Biomed. Opt. Express **9**(10), 4730–4754 (Oct 2018)
12. Wang, J., Zhang, M., Pechauer, A.D., Liu, L., Hwang, T.S., Wilson, D.J., Li, D., Jia, Y.: Automated volumetric segmentation of retinal fluid on optical coherence tomography. Biomed. Opt. Express **7**(4), 1577–1589 (Apr 2016)
13. Wilkins, G.R., Houghton, O.M., Oldenburg, A.L.: Automated segmentation of intraretinal cystoid fluid in optical coherence tomography. IEEE Transactions on Biomedical Engineering **59**(4), 1109–1114 (2012)